International Journal of Multiphysics
Volume 18, No. 2, 2024
ISSN: 1750-9548

Pressure Drop Analysis of Incompressible Laminar Flow in a Low Aspect-Ratio Packed Bed Using CFD Simulations

Maher Lakkaichi*, Nawel Outili and Abdeslam Hassen Meniai

Laboratory of environmental process engineering, Faculty of process engineering, University of Constantine 3, Constantine, +213, Algeria

*Corresponding author maher.lakkaichi@univ-constantine3.dz

Abstract

Computational Fluid Dynamics (CFD) is a worthwhile method for studying complex flows in packed bed reactors. The paper debates different CFD modeling approaches of incompressible laminar flow through packed beds with a particle to column diameter ratio of 2. Using COMSOL Multiphysics 5.6, five different cases have been simulated and compared in term of pressure drop. Excellent agreement was found between the proposed hypothetical and the resolved-particle (3D) models, mainly for the lower Inlet particle Reynolds numbers, with relative deviation of 3% and 7% at inlet Reynolds numbers of 27 and 55, respectively. Concerning the pseudo homogeneous cases, three different drag laws have been exercised and it has been found that applying the semi-empirical correlation, which takes into account the wall effects, in the flow equations showed the best agreement to the 3D model, with relative deviation being in the range 5%-25%. Considering these, one can recommend to use the proposed less computationally intensive approach or to apply the chosen drag law model in the momentum balance when designing a packed bed with aspect ratio of 2.

Keywords*: COMSOL Multiphysics, Drag law, Hypothetical, Low aspect-ratio, Packed-bed, Pressure drop, Resolved-particle.*

1. Introduction

Numerous industrial processes use packed bed reactors (PBRs) with low aspect ratio (AR), due to its straightforward configuration, low pressure drop, large interstitial velocities and high surface-to-volume ratios inducing enhanced heat and mass transfer phenomenon [1–3]. These low AR packed beds have been shown to be effective for various applications such as steam reforming, oxidative dehydrogenation, nuclear reactors, separators and compact heat exchangers [1,3–5]. Despite these important applications, the number of studies to understand the hydrodynamics in low AR packed bed systems is unfortunately very low, particularly for AR less than 3 [1,2]. Only few publications considering the hydrodynamics of these types of reactors are reported in the literature.

One of the most crucial elements that must be precisely predicted when designing a packed bed, crossed by a fluid, is pressure drop, since it affects the flow distribution, pumping power and operating expenditures [6,7]. Additionally, the reliability of the applied pressure drop correlation determines the validity of pseudo-homogeneous models for complex flow in packed beds and the accurate prediction of the average behavior of the entire bed [8,9].

With recent increases in computational power, computational fluid dynamics (CFD) has become a viable method to analyze the complex flows in packed beds. Such CFD analyses require Three-Dimensional (3D) models when incorporating the bed structure's complexities (Resolved-Particle) for assessing the local flow field [10,11]. In addition to the 3D Resolve-Particle models, 2D representative models are used in order to

reduce the computational cost. Although local hydrodynamic phenomena required by 3D Resolved-Particle models could not be properly seized by 2D models [12], global macroscopic parameters (such as pressure drop) may be predicted accurately by 2D models [10].

Actually, 2D simulations use the classical porous media approach where the packed bed is represented by a continuous and homogeneous porous medium [13–15] . The resistance source terms are applied as closure drag law models in the averaged Navier-Stokes equations [16]. The obtained sets of partial differential equations were solved for the macroscopic flow field in the PBR (i.e. 2D pseudo homogeneous models). The effect of the solid phase is incorporated in the model equations implicitly via the bed porosity and the implemented drag force sub-models. These closure relationships can influence considerably the computed values of pressure drop especially for PBRs with low aspect ratio.

In the present study, a 2D porosity distribution function was considered and three drag force-sub models were tested and implemented in the modified Navier-Stokes equations to account for the momentum transfer at the fluid-solid interfaces leading to three axisymmetric pseudohmogenoeous models. The drawback of this conventional modeling approach was its dependency on closure sub-models which were developed on the basis of parametric fitting which involves finding coefficients (parameters) using a data set covering a limited range of operating conditions. Also a new method was proposed and based on transforming the complex 3D structure into a conceptual 3D structure which preserved some geometrical information and could be properly and easily simplified and transformed into a representative 2D structure by cross section geometry operation as will be described, hereinafter. The main advantage of this new approach is that it did not rely on any closure sub-models.

2. Objectives

The main objectives of the present paper are to (1) assess different drag laws using a 2D CFD pseudo homogeneous model and (2) study the efficiency of the new modeling approach, using a conceptual geometry, versus 3D modeling of laminar liquid flow in a packed bed with an aspect ratio of 2.

The remainder of the paper is organized as follows: (1) Writing the mathematical model equations and carrying out the simulations on COMSOL Multiphysics 5.6; (2) Conduct a mesh independency study of the 3D simulations, following the procedure established by [17], to determine the asymptotic pressure drop values and (3) Investigate the effectiveness of 2D against 3D simulations by comparison of the simulated results, in term of pressure drop, for different inlet particle Reynolds numbers.

3. Methods

3.1. Geometries and meshing

Creating geometry and meshing process are prior steps in performing a reliable CFD simulation [18]. One of the promising CFD software is COMSOL Multiphysics which has the capability of creating and dividing geometries into elements that can be used for the discretization of a computing domain.

3.1.1. Geometries

Three different geometries were created according to the space dimension (2D or 3D) and the type of the CFD model (Pseudohomogeneous or Resolved-Particle). The created geometries are (1) a 3D real geometry of the packed bed, (2) a 2D geometry representing implicitly the bed domain and (3) a 2D geometry representing explicitly the bed domain.

3.1.1.1. Real 3D Geometry: Cylindrical column packed with spherical particles

Identical-sized spheres are used and put one at a time into a cylindrical column with a diameter twice as large as the particle diameter (d_p), so that one layer can accommodate only two tangent spheres. Then the first two spheres stand on the column base tangentially to its wall and their centerline passes through the center of the circular base of the column and is in a plane perpendicular to the column vertical axis. The next two spheres are arranged so that their centerline makes an angle of 90° with that of the two spheres of the previous layer [19].

This geometric arrangement is repeated for the subsequent layers up to the top of the bed [10] and can be represented by a number of repeating unit cells having the same overall properties, particularly an overall void fraction equal to that of the entire bed [19]. The height of a unit cell, denoted by h*, is related to the particle diameter, as follows:

$$h^* = \frac{dp}{\sqrt{2}} \quad (1)$$

The used total number of layers is 21 with a bed height to particle diameter ratio of about 15.14, which is sufficient to avoid column top and bottom effects on the porosity, although a desirable ratio should be greater than 20 [20,21].

To eliminate the entrance and the exit effects, the volume meshes was extended one cylinder diameter in the axial direction at the inlet and outlet [20] as shown in Figure 1a. The obtained results presented below confirm the fact that considering 21 layers and extending the total reactor length one cylinder diameter at the inlet and outlet, is sufficient for bulk unit cell pressure drop to reach a fully steady state. The spheres diameter was set to be equal 0.019 mm, but it was reduced by 1% to avoid unsuitable thin cells near the contact points between particles as well as between particles and the cylinder wall, which may induce solution convergence problems. Exploiting the symmetry of the system, simulations were run over one quarter of the geometrical domain to reduce the computational time.

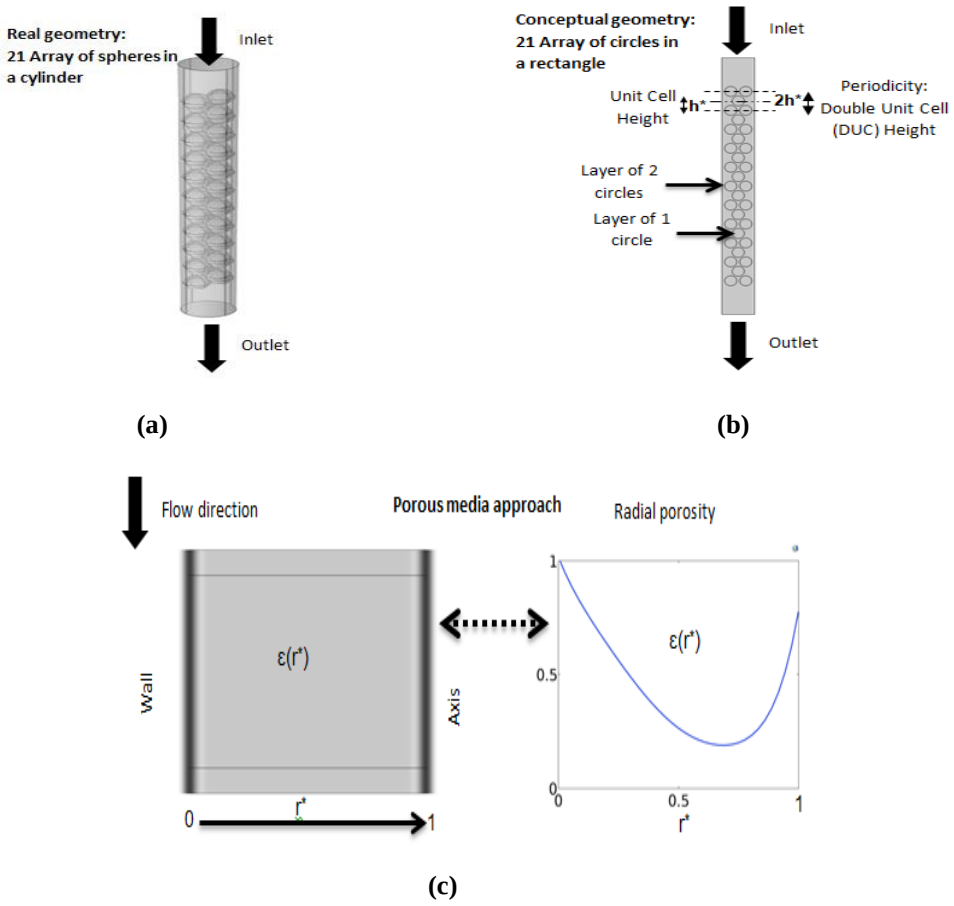

Figure 1: Geometries used in different modelling approaches: (a) Real geometry: Three-Dimensional Resolved-Particle Model (3D-RPM); (b) Conceptual geometry: Two-dimensional Resolved-Particle Model (2D-RPM); (c) Two-Dimensional axisymmetric: Pseudo-Homogeneous Model (2D-PHM).

3.1.1.2. 2D axisymmetric rectangle: Flow in an empty tube

Concerning the 2D pseudo homogeneous cases, there is no need to include any details of the bed structure, since the domain is considered continuous and homogeneous. In this case, the liquid is assumed to be flowing in an empty tube. Therefore, the geometry of the domain is rectangular as shown in Figure 1c. Based on the porous media approach, the effect of the bed textual properties on the flow is integrated into the transport equations via a porosity distribution function and drag force closure relationships.

3.1.1.3. 2D Rectangle containing a group of circles: Fictitious flow past an array of circular cylinders

Regarding the conceptual model, an imaginary 3D geometry was proposed, which is able to capture to some extent the explicit description of the textual characteristics of the real bed geometry and which can be easily simplified and transformed into a 2D geometry by using cross section geometry operation available in COMSOL Multiphysics 5.6 software. The proposed conceptual 3D geometry is a group of circular cylinders (hypothetical particles) positioned horizontally between two vertical and parallel plates, as if the cylindrical column (real bed) is bisected into two stretched halves. This similarity can be put forward for two considerations. Firstly, the circular shape of the hypothetical particles, in the conceptual geometry, may capture the circular curvature of the spherical particle in the real bed. Secondly, the vertical plates containing the cylindrical particles (in the conceptual geometry) could be consistent with the real column surrounding the spherical particles (in the real geometry). The height of the plates is the same as that of the cylindrical column and the distance between the two plates is equivalent to the bed diameter. The number, the position and the diameter of the circular cylinders determine the tortuous pattern and the void fraction in the new 3D geometry.

By using the cross section geometry operation on the conceptual 3D domain, a fictitious 2D geometry was created. This latter is represented by a rectangle containing 32 mono-sized circles, as shown in Figure 1b, which are located as follows:

- The *i*-th Layer containing two circles (*i*=1:11):

$$x_{2i-1} = -x_{2i-1} = \frac{dp}{3} \text{ and } y_{2i-1} = \frac{5dp}{2} + (2i-2)h^* \quad (2)$$

- The *j*-th Layer containing one circle (*j*=1:10):

$$x_{2j} = 0 \text{ and } y_{2j} = \frac{5dp}{2} + (2j-1)h^* \quad (3)$$

Where x and y are the coordinates of the circles center.

The hypothetical circle diameter is determined assuming that the hypothetical 2D unit cell porosity is equivlent to the real 3D unit cell porosity, as described in Appendix A. These mean that the circles locations and the overall void fraction are the main geometrical information required by the conceptual 2D geometry.

3.1.2. Meshing

Regarding the 3D modeling and due to the complex 3D geometry, the generated mesh consisted of free tetrahedral. Furthermore, to solve viscous effects, the meshing is refined in a boundary layer at the fluid-particles and fluid-walls interfaces, which include two boundary layers to enhance the cells quality, without an excessive cell count [22–24]. Finally, a corner refinement procedure was also implemented to further refine the mesh and get a better resolution of the corners and edges in narrow regions.

Similarly, in order to attain a high level accuracy of 2D simulations, the same meshing sequences were built, but free triangular shapes cells were used in the two dimensional domains.

In each of these studies, the mesh density was determined in a mesh independence study.

3.2. CFD modeling

3.2.1. Three and two-dimensional resolved particle models (3D-RPM and 2D-RPM)

The hydrodynamic model for both resolved-particle cases is described by Equations (4) and (5), which represent the continuity and the momentum balance equations, respectively.

$$\rho \nabla . \boldsymbol{u} = 0 \quad (4)$$

$$\rho(\boldsymbol{u}.\nabla)\boldsymbol{u} = \nabla.[-p\boldsymbol{I} + \mu(\nabla\boldsymbol{u} + (\nabla\boldsymbol{u})^T)] + \rho\boldsymbol{g} \quad (5)$$

Where ρ, μ and $\boldsymbol{g}$ are the fluid density, dynamic viscosity and gravity acceleration, respectively, $\boldsymbol{u}$ and p are the local velocity and pressure at any given position in the interstitial porous bed and in the extended inlet and outlet free volumes. Equation (5) is the standard Navier-Stokes equation for incompressible flow. Equations (4) and (5) were solved in the interstitial domain of the bed and the extended free domains, similarly to the model implementation carried out by Uribe and coworkers [24,25]. An important aspect to highlight on the implemented model is that there is no need to include any expressions for porosity distribution and fluid-solid drag [12,24,26,27], which is a common practice when implementing pseudo homogeneous models, since the implemented model explicitly includes these parameters via the solids distribution and the solid walls boundary conditions. Hence, the solid phase distribution is required by implemented geometries representation as described in Figures 1a and 1b, while the average fluid-solid interactions are assumed at the fluid-solid contact surface through setting the boundary conditions.

The boundary conditions set to the model were an inlet velocity (u_{in}), outlet pressure (p_{0ut}) and a non-slip condition at the column walls and at the fluid-solid interface (A_{fw}). Equations (6) to (8) describe the boundary conditions for equations (4) and (5).

$$\boldsymbol{u_{in}} = -U_{in}\boldsymbol{n} \quad \text{(inlet)} \quad (6)$$

$$[-p\boldsymbol{I} + \mu(\nabla\boldsymbol{u} + (\nabla\boldsymbol{u})^T)]\boldsymbol{n} = -p_{out}\boldsymbol{n} \quad \text{(outlet)} \quad (7)$$

$$\boldsymbol{u} = 0 \quad \text{(walls and } A_{fw}\text{)} \quad (8)$$

where U_{in} is the superficial inlet velocity. The boundary condition described by Equation (7) specifies that the normal stress at the reactor outlet is equal to the outlet pressure, which was set to be 1 atm. It can be seen from Equation (8) that the solids are considered as impermeable, and therefore a no-slip boundary condition is set at their surface.

In both resolved particle cases (I and II), which are illustrated in Table 1, the governing equations are the same, with the same physical properties, inlet, outlet and operating conditions. Thus, the possible differences in the macroscopic average behaviors, such as pressure drop, may result from differences between the real and the conceptual geometries.

Table 1: Simulated cases

Case N°	**Model type**	**Features**
I	Resolved-particle (Real geometry): 3D-RPM	Three-Dimensional No closure sub-models
II	Resolved-Particle (Conceptual geometry): 2D-RPM	Two-Dimensional No closure sub-models
III	Pseudo-homogeneous: 2D-PHM_Ergun	Two-Dimensional Semi-empirical drag law by (Ergun, 1952) Porosity distribution function by (Mueller, 2010)
IV	Pseudo-homogeneous: 2D-PHM_Tang	Two-Dimensional First principle-based drag law by (Tang et al., 2015) Porosity distribution function by (Mueller, 2010)
V	Pseudo-homogeneous:	Two-Dimensional

	2D-PHM_ES	Semi-empirical drag law by (Eisfeld and Schnitzlein, 2001) Taking into account the wall effects Porosity distribution function by (Mueller, 2010)

3.2.2. Pseudo homogeneous models (PHMs)

The hydrodynamic model for both pseudo homogeneous cases is described by Equations (9) and (10), which represent the continuity and the momentum balance equations, respectively.

$$\rho \nabla . \boldsymbol{U} = \boldsymbol{0} \tag{9}$$

$$\frac{1}{\varepsilon}\rho(\boldsymbol{U}.\nabla)\boldsymbol{U}\frac{1}{\varepsilon} = \nabla.\left[-P\boldsymbol{I} + \mu\frac{1}{\varepsilon}(\nabla\boldsymbol{U} + (\nabla\boldsymbol{U})^T)\right] + \left(\frac{\mu}{k_1} + \frac{\rho}{k_2}|\boldsymbol{U}|\right)\boldsymbol{U} + \rho\boldsymbol{g} \tag{10}$$

In these, $\boldsymbol{U}$ is the superficial average velocity, which is a hypothetical velocity of the flowing fluid in a free channel and P is an intrinsic average pressure. Actually, Equation (10) is the Navier-Stokes-Darcy-Forchheimer equation which is the modification of the original Navier-Stokes equation (Equation (5)) [12,28]. This modified transport equation includes additional terms, capturing the porous media information, which are the porosity (ε), the Darcian (k_1) and the non-Darcain (k_2) permeabilities.

Regarding the bed porosity, the analytical expression by [19] and the semi-analytical expression by [29] for the radial porosity distribution in packed bed with aspect ratio of 2 are benchmarks with existing experimental data for mono-sized spheres. The void fraction in the bed with aspect ratio equal to 2 begins at unity at the wall, decreases to a minimum of 0.19 at a distance of around $0.68d_p$ from the wall, and then increases to reach unity at the bed's axis (see Figure 1c). In fact, this geometrical parameter is an average property, so that the expressions that forecast radial variations are actually forecasting the average profile of an average property. This suggests that the predicted profiles might not actually have any physical significance, but they do allow for some partial capture of the influence of the bed structure on the averaged macroscopic parameter profiles [12].

The second important variable is permeability, which measures the capacity and the ability of a porous medium to transmit a fluid [30]. In another way, it measures the resistance to flow caused by the porous medium structure [12]. Actually, there exist two permeabilities as appearing in the right-hand side of Equation (10) which were well described as follows [18,31]:

$$k_1 = \frac{\varepsilon^3}{\alpha S_V^2(1-\varepsilon)^2} \tag{11}$$

$$k_2 = \frac{\varepsilon^3}{\beta S_V(1-\varepsilon)} \tag{12}$$

In these, $S_V = 6/d_p$ is the solid particles specific area, where α and β are the viscous and inertial parameters, respectively, defined by Equations (14) and (15).

Actually, the second term in the right side of Equation (10) may represent the pressure drop per unit length of the PBR and is a function of: (1) the flow rate, (2) the fluid viscosity and density (3) closeness and orientation of the packing and (4) size, shape and surface roughness of the particles. Hence, this term is very sensitive to the geometrical properties of the bed [20]. A number of methods exist to describe and predict the pressure drop over PBRs such as empirical relationships, capillary models, statistical models and hydraulic radius principles [30]. The most common method uses hydraulic radius concept to calculate the resistance to flow inside the bed. In this context, the well know drag force correlation by [32], states that the pressure drop per unit length of porous medium is the sum of viscous and inertial terms, which can be written as:

$$\frac{\Delta p}{L} = A_{Ergun}\frac{(1-\varepsilon)^2}{\varepsilon^3}\frac{\mu U_S}{{d_p}^2} + B_{Ergun}\frac{(1-\varepsilon)}{\varepsilon^3}\frac{\rho {U_S}^2}{d_p} \tag{13}$$

In Equation (13), A_{Ergun} and B_{Ergun} are the viscous and inertial Ergun constants, which are related to the viscous and inertial parameters in expressions (11) and (12), through the following equalities [18]:

$$A_{Ergun} = \alpha 36 = (2\alpha^*)36 = 150 \quad (14)$$

$$B_{Ergun} = \beta 6 = (\beta^*/8)6 = 1.75 \quad (15)$$

In these, $\alpha^*$and $\beta^*$are parameters which include the tortuosity factor and which could be determined theoretically or experimentally [18].

In recent years, advances of Particle Resolved-Direct Numerical Simulations (PR-DNS) have led to new correlations based on first principles [33]. Through PR-DNS the fluid-solid momentum transfer is modeled depending on the boundary conditions at the particles surface rather than on empirical hypotheses. What distinguishes PR-DNS is that, unlike experiments, arbitrary material and flow characteristics may be established and fully controlled in simulations [33–36]. Based on the Immersed Boundary condition Method (IBM), Tang (2015) developed an accurate drag law which is considered as the best possible expression of the drag force in static mono disperse arrays of spheres for $\mathrm{Rep} \leq 1000$ [36].

The disadvantage of both the semi empirical correlation by [32] and the first principle-based correlation by [36] is that they do not take the wall effects into account and present inaccurate predictions at aspect rations lesser than 10 [4,7]. It is noteworthy to mention that for low particle to column diameter ratios the column wall may affect the flow within the packed bed considerably through two opposite effects, notably a local increase in porosity near the wall and additional resistance due to the wall friction [4,7,8]. Therefore, many authors have attempted to improve these correlations to include the wall effect, by fitting semi-empirical correlations to their experimental data. One of the most promising correlations is the Eisfeld and Schnitzlein (ES) correlation which is an Ergun-type equation and which was derived from more than 2300 experimental data points [8]. This correlation is relevant to the current investigation since it takes the wall effect into consideration, and predicts accurate values of the friction factor at low aspect ratios [20].

COMSOL Mulitphysics uses the Forchheimer equation, to account for the momentum transfer term in Equation (10), which is written as follows [18,28]:

$$\frac{\Delta p}{L} = \frac{\mu}{k_1} U + \frac{c_F \rho}{\sqrt{k_1}} U^2 \quad (16)$$

Where c_F is the Forchheimer coefficient that account for inertia drag.

The first and the second terms in the right side in Equation (16) represent the viscous and the kinetic energy losses, respectively. Confronting this Equation with the momentum transfer term in equation (10), leads to the following equalities:

$$k_2 = \sqrt{k_1}/c_f \quad (17)$$

User defined function, in COMSOL Multiphysics, is used to define the Darcian permeability, k_1, and the Forchheimer coefficient, c_F of the three drag laws exercised in the 2D CFD pseudo homogeneous model (Equations 9 and 10), which are summarized in Table 2.

Table 2: Drag force sub-models

Drag law	**Darcian permeability** (k_1)	**Forchheimer coefficient** (c_f)	**Constants**
Ergun (1952)	$\frac{\varepsilon^3 {d_p}^2}{A_{Ergun}(1-\varepsilon)^2}$	$\frac{B_{Ergun}(1-\varepsilon)}{\varepsilon^3 d_p}\sqrt{k_1}$	$A_{Ergun} = 150$ $B_{Ergun} = 1.75$
Eisfeld and Schnitzlein (2001)	$\frac{\varepsilon^3 {d_p}^2}{eE^2(1-\varepsilon)^2}$	$\frac{E}{\acute{E}}\frac{(1-\varepsilon)}{\varepsilon^3 d_p}\sqrt{k_1}$	$e = 154$, $\acute{e} = 1.15$, $e'' = 0.87$ $E = 1 + \frac{2}{3\gamma(1-\varepsilon)}$,

			$\acute{E} = (\acute{e}\gamma^{-2} + e'')^2$
			$\gamma = 2$
Tang et al. 2015	$1/A_{Tang}$ [(1)]	B_{Tang} [(2)]	-

[(1)] $A_{Tang} = 180\frac{(1-\varepsilon)^2}{\varepsilon^3 {d_p}^2} + 18(1-\varepsilon)\frac{\varepsilon}{{d_p}^2}(1 + 1.5\sqrt{1-\varepsilon})$

[(2)] $B_{Tang} = 18(1-\varepsilon)(0.11(2-\varepsilon)(1-\varepsilon) - \frac{0.00456}{\varepsilon^4} + \left(0.169\varepsilon + \frac{0.0644}{\varepsilon^4}\right) {Re_p}^{-0.343})(\frac{1}{\varepsilon d_p})$

3.3. Numerical setup

Simulations were conducted using the steady-state incompressible solver for the laminar flow available in COMSOL Multiphysics 5.6. All models were tested at low particle Reynolds numbers (Re_p), ranging from $Re_p = 27$ to $Re_p = 111$, which correspond to laminar steady flow conditions [10]. The convergence was evaluated based on relative tolerance of 0.001. A consistent mesh independent study was performed for the 3D simulations (Case I) to ensure the accuracy of the results and to determine the asymptotic pressure drop values. Besides, 2D simulations were conducted on extremely-finer meshes, where the grid is refined in stages until no significant differences in results occur between successive grid refinement stages.

4. Results and discussion

4.1. Estimation of discretization errors of the 3D simulations

In the following, the discretization error estimates in the 3D simulations, in term of pressure drop, are calculated and reported. It is a way of validation when experimental data are scares or not available for comparison [17]. Assessing the accuracy of code and calculations requires that the grid is sufficiently refined to the extent that the solution is within the asymptotic range of convergence. This can be checked by observing two grid convergence index (GCI) values as computed over three grids as described in Appendix B. The GCI is a measure of the percentage the computed value is away from the asymptotic value. A small value of GCI indicates that the solution is within the asymptotic range. This can be further verified by fulfilling the solution accuracy condition written as follows [37]:

$$\frac{GCI_{32}}{r_{21}^m GCI_{21}} = 1 \quad (18)$$

Then the reason to trust the accuracy of a numerical simulation is validated and the solution is independent of the mesh size.

Table 3: Mesh independency study: Error estimates in 3D simulations, in term of pressure drop, at different inlet Rep values

Results	**Rep_in=27**	**Rep_in=55**	**Rep_in=111**
Asymptotic pressure drop value (Pa/m)	2.71	6.91	20.48
$\boldsymbol{GCI_{21}}$ **(%)**	0.23	0.84	4.44
$\frac{GCI_{32}}{r_{21}^m GCI_{21}}$ **(Solution accuracy condition)**	1.000	1.003	1.007

Table III displays results of asymptotic pressure drop, grid convergence index and a solution accuracy check for the tree inlet Rep values. Here, the pressure drop values were calculated in the bulk region of the bed where the flow is fully steady state as it will be demonstrated in the following section.

Overall, the solution accuracy ratio is almost equal to one for all the inlet Rep values, thus the solutions are within the asymptotic ranges of convergence. In term of grid convergence index, for all cases, GCI_{21} is lower than 4.5%, having the smallest value for Rep_in=27. The observed higher values of GCI_{21} for Rep_in=111, comparing to the other cases, could be attributed to the grid size not being able to capture all the information of the flow field. Using the asymptotic pressure drop values as well as their respective GCIs, the exact solutions of pressure drop through the packed bed may be written as:

$$\Delta P_{exact} = \Delta P_{asymp} \frac{(100 \pm GCI_{21})}{100} \tag{18}$$

3.2. Comparison of pressure drop simulated results

Predicted results of pressure drop by the 3D simulations (Case I) and the 2D simulations (Cases II-V) could be obtained by calculating the difference in the radially-averaged pressure between the inlet and outlet bed boundaries. However, to eliminate any entrance and exit effects on the results, pressure drop should be calculated between two stages in the bed within a region where the flow becomes fully steady state.

The geometrical domains were divided into a number of cut planes (for the 3D domain) or cut lines (for the 2D domains) with distances between two successive planes or lines of $z_{i+1} - z_i = h^*/10$ or $y_{i+1} - y_i = h^*/10$, respectively. Next, the pressures were measured by computing the average pressure on each cross section, at a level z or y. The elementary pressure drop results were then calculated by subtracting two sequential averaged pressure values.

Figures 2a, 2b and 2c show the change in frictional pressure drop, simulated by all cases, as a function of the normalized axial distance at inlet Rep values of 27, 55 and 111, respectively. It can be seen that for the three inlet Rep values tested, the observed behaviors of the five models are different.

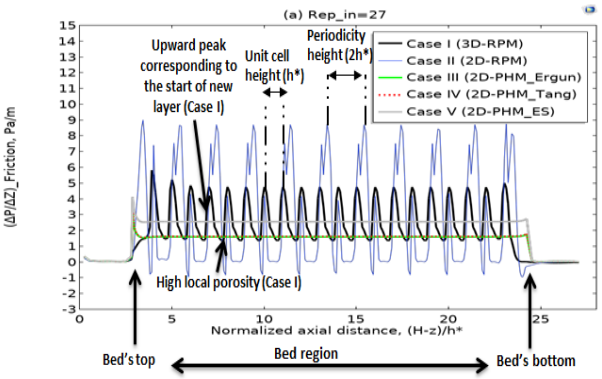

(a)

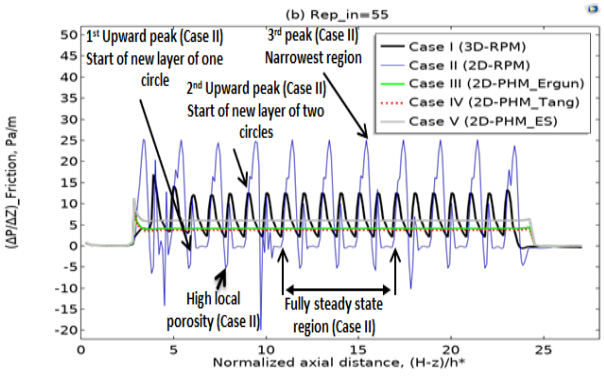

(b)

International Journal of Multiphysics
Volume 18, No. 2, 2024
ISSN: 1750-9548

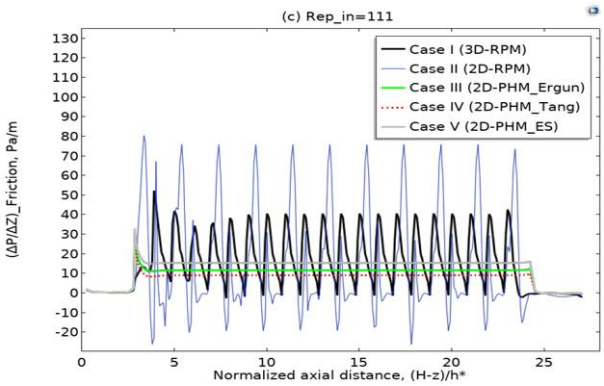

(c)

Figure 2: Comparison of frictional pressure drop simulated results as a function of

Concerning the pseudo homogeneous models, Cases (III, IV and V) show a smoother variation of the frictional pressure drop profile along the bed length. The observed peaks at the bed boundaries are due the transition between the free and the porous zones. Differently, both of the resolved-particle cases exhibit important fluctuations inside the bed region. These fluctuations are of a greater extent for Case II, which are generated by substantial variations in the textual characteristics of the fictitious 2D geometry comparing to the real domain in Case I. Each upward peak of Case I coincides with the start of a new layer. Similarly, each first and second upward peak in Case II coincides with the start of new layers containing one and two circles, respectively. Additionally, while the peaks in Case I and the third peaks in Case II correspond to the narrowest regions within the bed, the low points in both cases coincide with high local porosity regions. Moreover, it can be seen clearly that while the black curves show a periodicity every regular interval of one unit cell height, the blue one exhibits it every regular interval of Double Unit Cell (DUC) height. Furthermore, the height of the repeating parts, of both curves, becomes stable toward the bulk region of the bed where the flow is becoming fully steady state (see Figure 2b and Figure 3b), which means that the averaged pressure drops, for both cases, over a DUC height become constants within the bulk region of the bed, where any entrance and exit effects may be eliminated.

Figures 3a, 3b and 3c give information about the variation in frictional pressure drop every double unit cell height within the bed region, for all cases at inlet particle Reynolds number of 27, 55 and 111, respectively. As initial remark, simulated frictional pressure drop has to some extent similar trends for all the models and for all the three inlet Rep values.

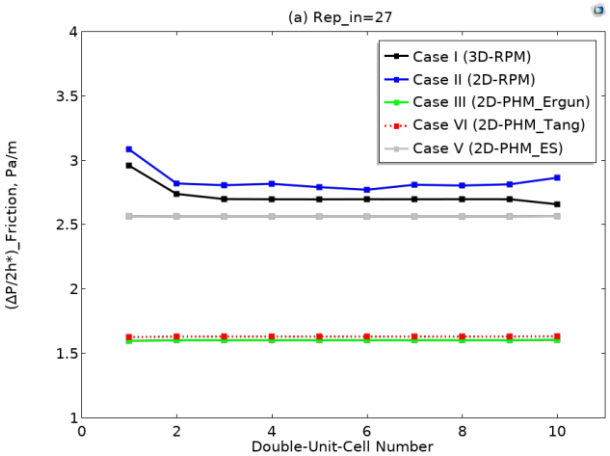

(a)

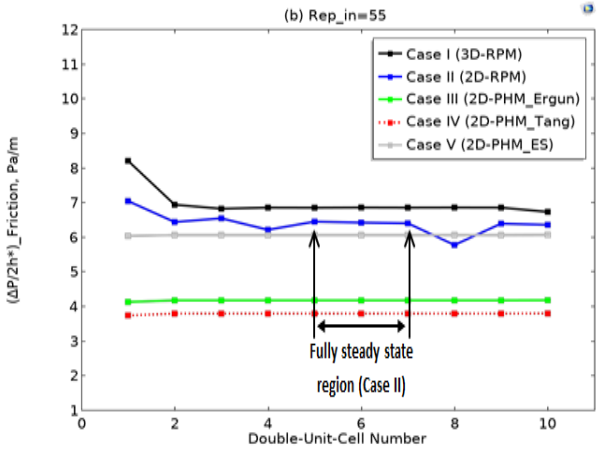

(b)

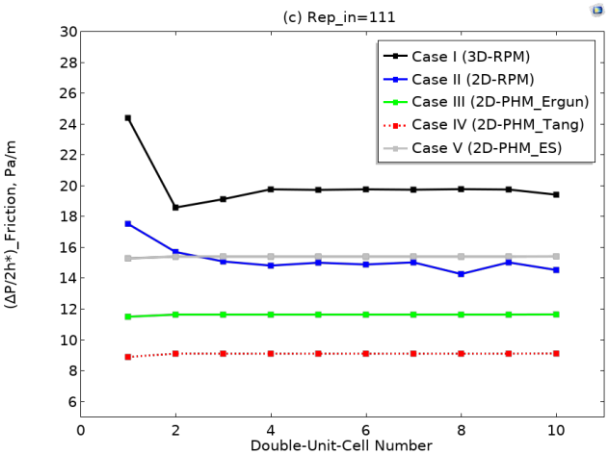

(c)

Figure 3: Comparison of frictional pressure drop simulated results as a function of Double-Unit-Cell number for all cases at different inlet Rep values: (a) 27; (b) 55; (c) 111.

All the pseudo homogeneous cases show constant Double-Unit-Cell (DUC) pressure drop profiles (ΔP/2h*) between the second DUC and the last DUC, which are represented by straight lines. The lower values through the first DUC are attributed to the redistribution of flow toward the low local porosity regions, mainly near the column wall. These variations are of greater extent in the resolved-particle Cases (I and II), which exhibit more instability of the DUC pressure drop simulated results within the bed region compared to the pseudo homogeneous Cases (III, IV and V). This may be explained by the strong influence of the bed's textual characteristics in the Resolved-Particle cases. Although, for both cases, the simulated DUC pressure drop level out in the bulk region of the bed, where any impacts of the bed's entrance and exit can be eliminated, mainly for Case I. For instance, simulated DUC pressure drop profile by Case II is stable between the fifth and the seventh DUC, as shown in Figure 3b, which correspond to the eighth and the fourteenth layers, as shown in Figure 2b. Therefore, to make an effective comparison between all cases, the DUC pressure drop should be calculated in the middle of the bed, to eliminate any entrance and exit effects.

The bar chart, in figure 4, illustrates the mean relative deviation (MRD) of the predicted pressure drop results by the 2D simulations (Cases II, III, IV and V) with respect to the 3D simulations (Case I) for inlet particle Reynolds numbers of 27, 55 and 111.

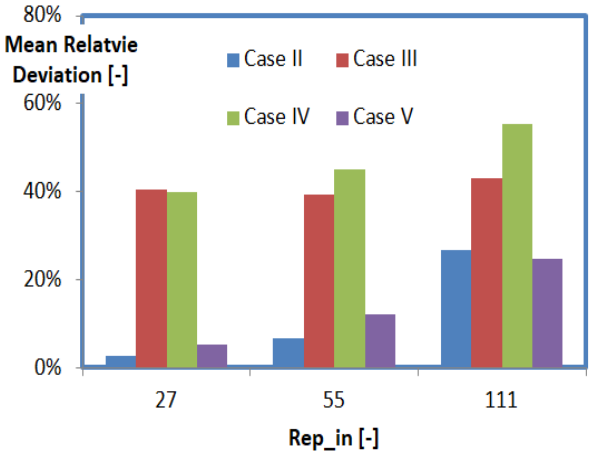

Figure 4: Mean Relative Deviation (MRD) of the simulated pressure drop results in Cases (II, III, IV and V) in reference to Case I at different inlet Rep values.

Overall, Case II and to a lower extent Case V showed the best fits to Case I, concerning the bulk pressure drop, for all the inlet Rep values. In Case II, the MRD was about 3% at inlet Rep of 27, then it increased to around 7%

at inlet Rep of 55, being the lowest values, and continued to increase reaching almost 27% at inlet Rep of 111. Similarly, the MRD by Case V was about 5% at inlet Rep of 27, and then it rose to around 12% at inlet rep of 55, being the second lowest values, and increased further achieving nearly 25% at inlet Rep of 111. While, the MRD for both Cases (II and V) did not exceed 27% for all the inlet Rep tested, the MRDs by Cases (III and IV) did not fall below 39%.These findings can be explained by the wall effects, which is well taken into consideration by Case II, through the 2D imaginary geometry, and by Case V, using the ES semi-empirical correlation.

5. Conclusion

The simulation of the considered five different cases (a Three-Dimensional Resolved-Particle, a Two-Dimensional Resolved-Particle (conceptual) and three Pseudo-homogeneous and incompressible flow) in a packed bed with aspect ratio of 2, for three inlet particle Reynolds numbers of 27, 55 and 111, corresponding to the laminar flow regime, was a good contribution to the study of the efficiency of different drag laws when implemented in a 2D CFD pseudo homogeneous model and to the investigation of the efficacy of a new CFD modeling approach.

Clearly the comparison of the obtained results, in term of pressure drop, indicated that the proposed approach in Case II, using a conceptual geometry, and to a smaller extent in Case V, using the ES correlation, showed the best fit to the 3D model where the maximum MRD did not Exceed 27% at inlet Rep of 111. An excellent agreement was found at lower inlet Rep values, where the MRDs of Cases II and V varied between 3 and 5% at Rep_in = 27 to 7% and 12% at Rep_in=55, respectively. Summing up the results, it can be concluded that considering the conceptual 2D geometry or applying the ES correlation in the flow equations when designing a packed bed with aspect ratio of 2, may give accurate results with lesser computing time comparing with 3D simulations.

Clearly, future work will be needed to validate our new approach when coupling hydrodynamics with chemical reactions.

As the industry that depends on these type of packed bed reactors with low aspect ratio is becoming more concerned all over the world, any additional contribution to its design and/or modeling of various parameters will not only lead to technology progress, resulting in significant savings, but will also help to protect the environment.

Appendices

Appendix A

The hypothetical 2D unit cell porosity can be defined according to Equation A1

$$\varepsilon_{2D} = \frac{\frac{3}{2}S_C}{S_{\_2D-UC}} \tag{A1}$$

Where S_C and $S_{\_2D-UC}$ are the surface areas of one circle and the hypothetical 2D unit cell (2D-UC) in the conceptual geometry, which may be given by:

$$S_C = \frac{\pi}{4} {d_c}^2 \tag{A2}$$

$$S_{\_2D-UC} = 2dph^* \tag{A3}$$

Where d_c is the diameter of a hypothetical circular particle.

Let the 3D unit cell porosity be given by

$$\varepsilon_{3D} = \frac{\frac{3}{2}V_p}{V_{3D-UC}} \tag{A4}$$

Where V_p and V_{3D-UC} are the particle and the unit cell volumes (in the real bed), which may be given by:

$$V_p = \frac{\pi}{6} dp^3 \quad \text{(A5)}$$

$$V_{3D-UC} = \pi dp^2 h^* \quad \text{(A6)}$$

Assuming that ε_{2D} and ε_{3D} are equals, the circle diameter can be derived according to (A7)

$$d_c = 2\sqrt{\frac{1}{3\pi}} dp \quad \text{(A7)}$$

Appendix B

To ensure that the results are independent of mesh size, the numerical errors of the simulations were analyzed using the procedure provided by (17). Let us first define the representative grid size *h*, for three-dimensional space, by

$$h = \left[\frac{1}{N}\sum_{k=1}^{N}(\Delta V_k)\right]^{1/3} \quad \text{(B1)}$$

where ΔV_k is the volume of the *k*th cell and *N* is the total number of cells used for computations. Three gird sizes were selected such that, the grid refinement factors, defined by Equation (B2) and (B3), should be greater than 3.

$$r_{21} = \frac{h_2}{h_1} \quad \text{(B2)}$$

And

$$r_{32} = \frac{h_3}{h_2} \quad \text{(B3)}$$

Then, the expression that defines the apparent order of the method is as follows:

$$p = \frac{1}{ln\, r_{21}} \left| ln \left| \frac{\theta_{32}}{\theta_{21}} \right| + q(p) \right| \quad \text{(B4a)}$$

$$q(p) = \ln\left(\frac{r_{21}^{P} - s}{r_{32}^{P} - s}\right) \quad \text{(B4b)}$$

$$s = 1.\, sgn\left(\frac{\theta_{32}}{\theta_{21}}\right) \quad \text{(B4c)}$$

In these, $\theta_{32} = (\Delta P)_3 - (\Delta P)_2$ and $\theta_{21} = (\Delta P)_2 - (\Delta P)_1$ with$(\Delta P)_1$, $(\Delta P)_2$ and $(\Delta P)_3$ are the simulated pressure drop results using the three grid sizes h_1, h_2 and h_3, respectively.

Finally, the asymptotic pressure drop and its associated Grid Convergence Index on the finer grid (GCI_{21}), may be calculated as follows:

$$(\Delta P)_{Asymp} = \frac{(r_{21}^{P}(\Delta P)_1 - (\Delta P)_2)}{(r_{21}^{P} - 1)} \quad \text{(B5)}$$

$$GCI_{21} = \frac{1.25 e_{21}}{r_{21}^{P} - 1} \quad \text{(B6)}$$

References

[1] Alzahrani F, Aldehani M, Rusi H, McMaster M, Abreu Fernandes DL, Assabumrungrat S, et al. Gas flow visualization in low aspect ratio packed beds by three-dimensional modeling and near-infrared tomography. Industrial & Engineering Chemistry Research 2015;54:12714–29. https://doi.org/10.1021/acs.iecr.5b02635.s002.

[2] Guo Z, Sun Z, Zhang N, Ding M, Wen J. Experimental characterization of pressure drop in slender packed bed (1< D/d< 3). Chemical Engineering Science 2017;173:578–87. https://doi.org/10.1016/j.ces.2017.08.022.

[3] Romero-Limones A, Poissonnier J, Thybaut JW, Castillo-Araiza CO. A pseudo-local heat transfer approach in a low tube to particle diameter ratio packed bed catalytic reactor: Oxidative dehydrogenation of ethane as a case study. Chemical Engineering Journal 2023;454:140392. https://doi.org/10.2139/ssrn.4173893.

[4] Freund H, Zeiser T, Huber F, Klemm E, Brenner G, Durst F, et al. Numerical simulations of single phase reacting flows in randomly packed fixed-bed reactors and experimental validation. Chemical Engineering Science 2003;58:903–10. https://doi.org/10.1016/s0009-2509(02)00622-x.

[5] Pistocchini L, Garone S, Motta M. Fluid dynamics optimization of a novel isothermal adsorption dehumidification system for solar driven applications. Energy Procedia 2014;48:1689–98. https://doi.org/10.1016/j.egypro.2014.02.073.

[6] Das S, Deen NG, Kuipers JAM. A DNS study of flow and heat transfer through slender fixed-bed reactors randomly packed with spherical particles. Chemical Engineering Science 2017;160:1–19. https://doi.org/10.1016/j.ces.2016.11.008.

[7] Hassan YA, Kang C. Pressure drop in a pebble bed reactor under high Reynolds number. Nuclear Technology 2012;180:159–73. https://doi.org/10.13182/nt12-a14631.

[8] Eisfeld B, Schnitzlein K. The influence of confining walls on the pressure drop in packed beds. Chemical Engineering Science 2001;56:4321–9. https://doi.org/10.1016/S0009-2509(00)00533-9.

[9] Reger D, Merzari E, Balestra P, Schunert S, Hassan Y, Yuan H. An improved pressure drop correlation for modeling localized effects in a pebble bed reactor. Nuclear Engineering and Design 2023;403:112123. https://doi.org/0.1016/j.nucengdes.2022.112123.

[10] Robbins DJ, El-Bachir MS, Gladden LF, Cant RS, von Harbou E. CFD modeling of single-phase flow in a packed bed with MRI validation. AIChE Journal 2012;58:3904–15. https://doi.org/10.1002/aic.13767.

[11] Micale D, Ferroni C, Uglietti R, Bracconi M, Maestri M. Computational fluid dynamics of reacting flows at surfaces: Methodologies and applications. Chemie Ingenieur Technik 2022;94:634–51. https://doi.org/0.1002/cite.202100196.

[12] Uribe S, Qi B, Cordero ME, Al-Dahhan M. Comparison between pseudohomogeneous and resolved-particle models for liquid hydrodynamics in packed-bed reactors. Chemical Engineering Research and Design 2021;166:158–71. https://doi.org/0.1016/j.cherd.2020.12.001.

[13] Bded. Performance Simulation for Gas Flow through a Porous Media in Packed bed Columns using CFD. IOP Conference Series: Materials Science and Engineering 2001;579:01. https://doi.org/10.1088/1757-899X/579/1/012001.

[14] George GR, Bockelmann M, Schmalhorst L, Beton D, Gerstle A, Torkuhl L, et al. Workflow for computational fluid dynamics modeling of fixed-bed reactors packed with metal foam pellets: Hydrodynamics. AIChE Journal 2023;69:e17284.

[15] Ranade VV, Chaudhari RV, Gunjal PR. Trickle bed reactors: reactor engineering & applications. Amsterdam: Elsevier; 2011.

[16] Crolet J-M. Computational methods for flow and transport in porous media 2013. https://doi.org/10.1016/j.cej.2010.10.053.

[17] Celik IB, Ghia U, Roache PJ, Freitas CJ. Procedure for estimation and reporting of uncertainty due to discretization in CFD applications. Journal of Fluids Engineering-Transactions of the ASME 2008;130. https://doi.org/10.1115/1.2960953.

[18] Pavlišič A, Pohar A, Likozar B. Comparison of computational fluid dynamics (CFD) and pressure drop correlations in laminar flow regime for packed bed reactors and columns. Powder Technology 2018;328:130–9. https://doi.org/0.1016/j.powtec.2018.01.029.

[19] Govindarao VM, Ramrao KV, Rao AV. Structural characteristics of packed beds of low aspect ratio. Chemical Engineering Science 1992;47:2105–9. https://doi.org/10.1016/0009-2509(92)80330-F.

[20] Van der Merwe WJS. Analysis of flow through cylindrical packed beds with small cylinder diameter to particle diameter ratios. North-West University, Potchefstroom Campus, 2014.

[21] von Seckendorff J, Achterhold K, Pfeiffer F, Fischer R, Hinrichsen O. Experimental and numerical analysis of void structure in random packed beds of spheres. Powder Technology 2021;380:613–28. https://doi.org/10.1016/j.powtec.2020.11.026.

[22] Eppinger T, Seidler K, Kraume M. DEM-CFD simulations of fixed bed reactors with small tube to particle diameter ratios. Chemical Engineering Journal 2011;166:324–31.

[23] Preller ACN. Numerical modelling of flow through packed beds of uniform spheres. North-West University, Potchefstroom Campus, 2011.

[24] Uribe S, Al-Ani M, Cordero ME, Al-Dahhan M. Modelling and validation of TBR Hydrodynamics: Local comparison between CFD and experiments. Fuel 2020;277:118244. https://doi.org/10.1016/j.fuel.2020.118244.

[25] Uribe S, Cordero ME, Reyes EP, Regalado-Méndez A, Zárate LG. Multiscale CFD modelling and analysis of TBR behavior for an HDS process: Deviations from ideal behaviors. Fuel 2019;239:1162–72. https://doi.org/10.1016/j.fuel.2018.11.104.

[26] Du Toit CG. Radial variation in porosity in annular packed beds. Nuclear Engineering and Design 2008;238:3073–9. https://doi.org/10.1016/j.nucengdes.2007.12.018.

[27] van Antwerpen W d, Du Toit CG, Rousseau PG. A review of correlations to model the packing structure and effective thermal conductivity in packed beds of mono-sized spherical particles. Nuclear Engineering and Design 2010;240:1803–18. https://doi.org/10.1016/j.nucengdes.2010.03.009.

[28] Amiri L, Ghoreishi-Madiseh SA, Hassani FP, Sasmito AP. Estimating pressure drop and Ergun/Forchheimer parameters of flow through packed bed of spheres with large particle diameters. Powder Technology 2019;356:310–24. https://doi.org/10.1016/j.powtec.2019.08.029.

[29] Mueller GE. Radial porosity in packed beds of spheres. Powder Technology 2010;203:626–33. https://doi.org/10.1016/j.powtec.2010.07.007.

[30] Taheri S, Ghomeshi S, Kantzas A. Permeability calculations in unconsolidated homogeneous sands. Powder Technology 2017;321:380–9. https://doi.org/10.1016/j.powtec.2017.08.014.

[31] Ergun S, Orning AA. Fluid flow through randomly packed columns and fluidized beds. Industrial & Engineering Chemistry 1949;41:1179–84. https://doi.org/10.1021/ie50474a011.

[32] Ergun S. Fluid flow through packed columns. Chem Eng Prog 1952;48:89–94. https://doi.org/10.1021/ie50474a011.

[33] Hardy B, Simonin O, De Wilde J, Winckelmans G. Simulation of the flow past random arrays of spherical particles: Microstructure-based tensor quantities as a tool to predict fluid–particle forces. International Journal of Multiphase Flow 2022;149:103970. https://doi.org/10.1016/j.ijmultiphaseflow.2021.103970.

[34] Beetstra R, van der Hoef MA, Kuipers JAM. Drag force of intermediate Reynolds number flow past mono-and bidisperse arrays of spheres. AIChE Journal 2007;53:489–501. https://doi.org/10.1002/aic.11065.

[35] Tenneti S, Garg R, Subramaniam S. Drag law for monodisperse gas–solid systems using particle-resolved direct numerical simulation of flow past fixed assemblies of spheres. International Journal of Multiphase Flow 2011;37:1072–92. https://doi.org/10.1016/j.ijmultiphaseflow.2011.05.010.

[36] Y. Tang Y, (Frank) Peters E, (Hans) Kuipers JAM, (Sebastian) Kriebitzsch SHL, (Martin) van der Hoef MA. A new drag correlation from fully resolved simulations of flow past monodisperse static arrays of spheres. AIChE Journal 2015;61:688–98. https://doi.org/10.1002/aic.14645.

[37] Examining Spatial (Grid) Convergence n.d. https://www.grc.nasa.gov/www/wind/valid/tutorial/spatconv.html (accessed July 19, 2023).